Acoustically induced electric and magnetic polarizations and theire sensing applications

Kenji Ikushima*

Department of Biomedical Engineering, Tokyo University of Agriculture and Technology, Nakacho, Koganei, Tokyo 184-8588, Japan

A measurement technique for detecting acoustically induced polarization is reviewed. Ultrasonic irradiation can generate alternating electric or magnetic polarization in materials via electromechanical or magnetomechanical coupling, respectively, and electromagnetic fields are often emitted to the surrounding environment when materials are acoustically stimulated. The linear response of the acoustically stimulated electromagnetic (ASEM) field is detected by a resonant antenna tuned to the ultrasound frequency. The ASEM response is generated in not only inorganic crystals but also biological tissues such as bones, tendons, and the aortic wall. The response signal is explained well by stress-induced electric polarization, which depends on the crystallinity of fibrous proteins. Ultrasound can temporally modulates the magnetic polarization (magnetization) in ferromagnetic materials, resulting in magnetic imaging and hysteresis measurements via ultrasonic stimulation. Therefore, probing ASEM responses opens possibilities for unique noninvasive sensing in medicine and industry.

1. Introduction

The fundamentals of physical acoustics developed greatly from the 1960s to the 1980s with the development of radio wave techniques, and the interaction of sound waves with various materials has been investigated, including the absorption mechanism of sound waves in solutions, metals, and semiconductors, and the coupling with spin systems and acoustically induced spin resonance in ferromagnetic materials.[1)] All this knowledge about physical acoustics is now being utilized in various fields, such as surface acoustic wave devices, magnetostrictive actuators, and acousto-optic devices, in combination with other advanced technology.

Meanwhile, ultrasound measurements —as typified by the echo method —are used widely in medical and industrial fields. Academic societies related to ultrasound techniques go far beyond the field of physics and are found in various fields such as medicine, the steel industry, and civil engineering, and measurement techniques for specific targets are being improved all the time. Why ultrasound techniques are used in such a wide range of practical settings may be

*E-mail: ikushima@cc.tuat.ac.jp

because (i) noninvasive evaluation is possible for many optically opaque objects and (ii) real-time waveform acquisition is easy in the radio frequency (rf) range. However, because ordinary ultrasound measurements acquire the reflection and transmission coefficients or velocity of the ultrasound, their use is limited mainly to evaluating mechanical properties and geometric anomalies; in other words, the electric and magnetic properties of materials are not probed.

Over the past decade, we have pursued a unique method for probing the electromagnetic properties of materials through ultrasound waves, known as the acoustically stimulated electromagnetic (ASEM) method.[2–5] In general, elastic waves do not couple directly with electric or magnetic properties. However, elastic modulation can often modulate the electric or magnetic polarization of an object temporally through electromechanical or magnetomechanical coupling, respectively. Therefore, it follows that rf dipole fields are emitted from the object to the surrounding environment when the object is acoustically stimulated [Fig. 1].

We have developed a measurement scheme that probes the ASEM field, which has not been available before, and have been studying the electric and magnetic polarizations induced by ultrasound waves. First, we revealed that ultrasound can electrically polarize not only inorganic piezoelectric crystals but also biological tissues such as bones, tendons, and the aortic wall.[3] Second, we showed that ultrasound can temporally modulate the magnetic polarization (magnetization) in ferromagnetic materials, resulting in magnetic imaging and hysteresis measurements via ultrasonic stimulation.[4,5] Herein, we present (i) the measurement concept of the ASEM method, (ii) what it can currently measure, and (iii) prospects for its sensing applications.

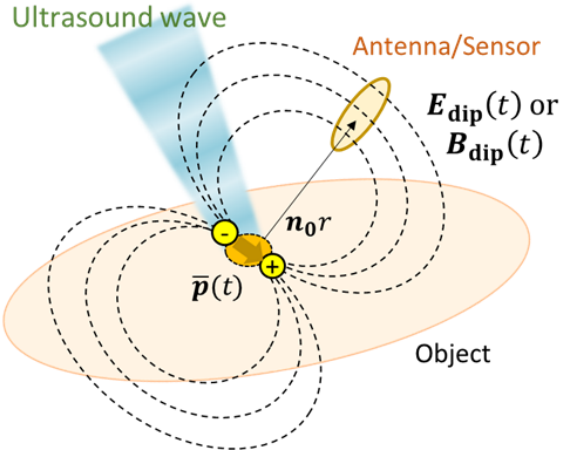

Fig. 1. Schematic of acoustically stimulated electromagnetic (ASEM) fields.

2. Measurement concept

Piezoelectric materials are discussed here, but piezomagnetic and ferromagnetic materials can be discussed similarly. Under adiabatic conditions, the applicable mechanical and electric equations of state for the piezoelectric medium can be written as

$$\begin{aligned} S_i &= s_{ij}T_j + d_{mi}E_m, \\ D_m &= d_{mi}T_i + \epsilon_{mk}E_k, \end{aligned} \tag{1}$$

where S, T, E, and D are the strain, stress, electric field, and electric flux density, respectively ($i, j = 1, 2, \ldots, 6$; $k, m = 1, 2, 3$). The coefficients relating the quantities $s_{ij} = (\partial S_i/\partial T_j)_E$, $d_{mi} = (\partial D_m/\partial T_i)_E = (\partial P_m/\partial T_i)_E$, and $\epsilon_{mk} = (\partial D_m/\partial E_k)_T$ are the elastic compliance, piezoelectric constant, and dielectric constant, respectively, where P is the electric polarization. Electrostriction (resp., magnetostriction) is phenomenologically equivalent to piezoelectricity (resp., piezomagnetism) in the linear response regime, and we make no distinction between them for the purpose of this discussion.[6)]

As defined originally, piezoelectricity was limited to single crystals of inorganic materials with no center of symmetry.[7)] Later, the concept of piezoelectricity was extended to polycrystals, organic materials,[8)] and even biological tissues.[9–13)] In the case of polycrystals, piezoelectric polarization can be attributed to the sum $\overline{\boldsymbol{p}}(t) = \sum_n \boldsymbol{p}_n$ of the electric dipole moments $\boldsymbol{p}_n$ occurring in partially crystalline regions within the material.

The local flux density $D_{\mathrm{loc}}(t)$ is temporally modulated via Eq. (1) when stress $T_{\mathrm{ac}}(t)$ is applied locally by ultrasonic irradiation. Consequently, the linear response (the first harmonic component) of locally induced polarization, that is, $P_{\mathrm{loc}}(t) = \overline{p}(t)/V = d_{\mathrm{loc}}T_{\mathrm{ac}}(t)$, oscillates at the ultrasound frequency in the acoustically excited volume V. The alternating electric dipole field emitted to the surrounding environment is then expressed as

$$\boldsymbol{E}_{\mathrm{dip}}(\boldsymbol{x}, t) = \frac{1}{4\pi\epsilon_0}\frac{3\boldsymbol{n}_0(\boldsymbol{n}_0 \cdot \overline{\boldsymbol{p}}(t)) - \overline{\boldsymbol{p}}(t)}{r^3}, \tag{2}$$

where $\boldsymbol{x} = \boldsymbol{n}_0 r$ is the vector from the position of the electric dipole moment to the observation point at distance r (on the order of centimeters), and ϵ_0 is the vacuum permittivity. This acoustically induced electric dipole field, which corresponds to the ASEM field, is detected by using a resonant capacitive antenna.

In the case of magnetism, E and D in Eq. (1) can be replaced by the magnetic field H and magnetic flux density B, respectively, P_{loc} and d_{loc} can be regarded as the local magnetization M and local piezomagnetic constant, respectively, and $\overline{\boldsymbol{p}}(t)$ can be replaced by $\overline{\boldsymbol{m}}(t)$, the sum of magnetic dipole moments in the acoustically excited volume. The alternating magnetic

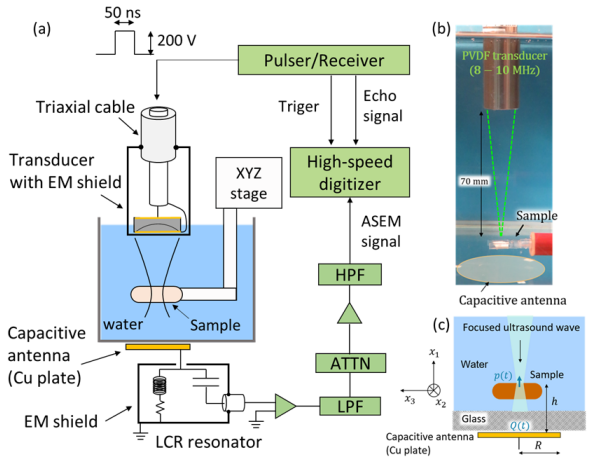

Fig. 2. (a) Block diagram of the experimental setup for measuring acoustically induced electric polarization.[3)] (b) Photograph of the setup. (c) Schematic of the geometric placement in the sample setting.

dipole field emitted to the surrounding environment is then expressed as

$$\boldsymbol{B}_{\mathrm{dip}}(\boldsymbol{x},t) = \frac{\mu_0}{4\pi}\frac{3\boldsymbol{n_0}(\boldsymbol{n_0}\cdot\overline{\boldsymbol{m}}(t)) - \overline{\boldsymbol{m}}(t)}{r^3}, \tag{3}$$

where μ_0 is the permeability of free space. The acoustically induced magnetic dipole field, which also corresponds to the ASEM field, is detected by a resonant loop antenna.

3. Acoustically induced electric polarization

3.1 Measuring and analysis method

A block diagram of the measurement setup is shown in Fig. 2.[3,14)] An appropriate distance between the sample and the transducer (70 mm) allows us to temporally separate the pulsed ASEM response from the electromagnetic noise generated by the transducer. For the transducer used in this experiment (made of polyvinylidene fluoride), its focal spot has a radius of ca. 0.65 mm and is on the surface of the sample. The rf ASEM field is detected by a resonant capacitive antenna tuned to the ultrasound frequency (8-10 MHz); the antenna is a copper plate coupled with an LCR resonator, and signals picked up by it are amplified and averaged at a repetition frequency of 1 kHz.

We began by investigating the ASEM field in some well-known inorganic crystals. Figure 3 shows time traces of the echo and ASEM signals for piezoelectric quartz and nonpiezoelectric silicon crystals. No explicit signal was observed in the silicon crystal [Fig. 3(c)], whereas a large signal was observed in the quartz crystal [Fig. 3(b)]. Because the ASEM signal is generated at half the echo delay time $\tau_{\mathrm{echo}}/2$, the signal observed at 47 μs is identified as the target response field of the quartz sample [Fig. 3(b)]. This indicates strongly that the ASEM

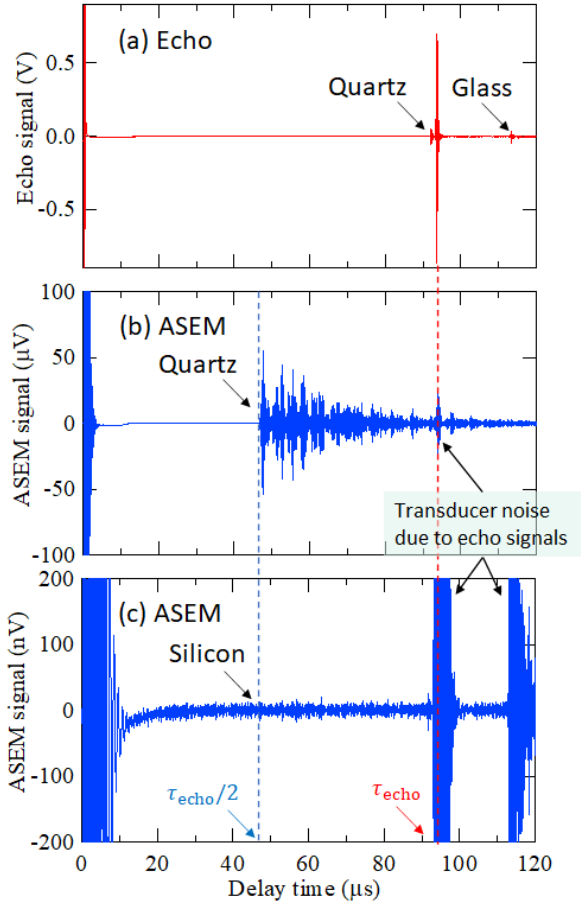

Fig. 3. (a) Time trace of echo signals in a piezoelectric quartz crystal (AT cut; diameter: 12.4 mm, thickness: 0.33 mm), and time traces of ASEM signals in (b) the quartz crystal and (c) a nonpiezoelectric silicon crystal (a 0.38-mm-thick 3 inch un-doped Si(100) wafer). The signals were averaged over 100 pulses for the quartz crystal and 3×10^4 pulses for the silicon crystal, and those around 94 μs and 114 μs are transducer noise due to echo signals from the quartz sample and the glass of the water tank, respectively.

signal is due to the piezoelectricity of the material. Similar results were also reported for piezoelectric GaAs in Ref. 2.

Here, we explain the dipole detection model for the quantitative analysis of acoustically induced electric polarization. Suppose that a surface charge $Q(t) = Q_0 \sin \omega_0 t$ is induced on a metal plate by an electric dipole moment $\overline{p}(t) = q_{\mathrm{dip}}(t)l$ [Fig. 4], where l is the displacement between the opposite charges $\pm q_{\mathrm{dip}}(t)$ and is on the order of half the ultrasound wavelength. Using the image dipole method [Fig. 4(a)], the electrostatic potential arising from the dipole moment, $\overline{p}$, is written as

$$V(x_1, x_2, x_3) = -\frac{1}{4\pi\epsilon_0}\left[\frac{\overline{p}(h - x_1)}{\{(x_1 - h)^2 + x_2^2 + x_3^2\}^{3/2}}\right.$$

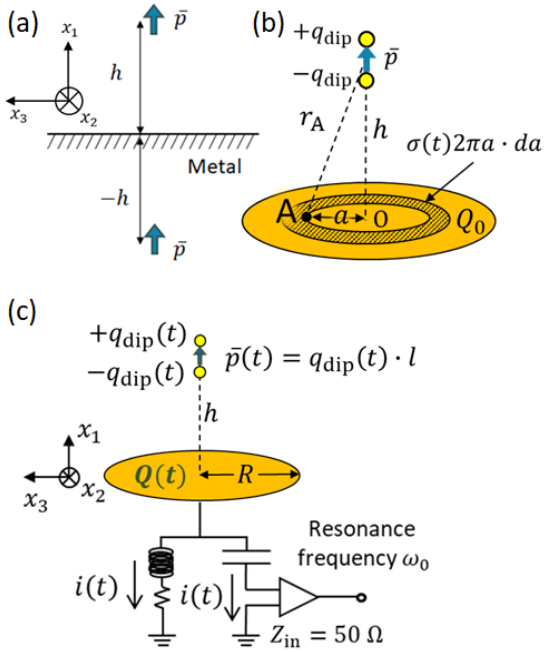

Fig. 4. Schematics of (a) the image dipole, (b) the induced surface charge $Q(t) = Q_0 \sin \omega_0 t$, on a metal plate due to the dipole, and (c) the detection circuit for the ASEM signal.

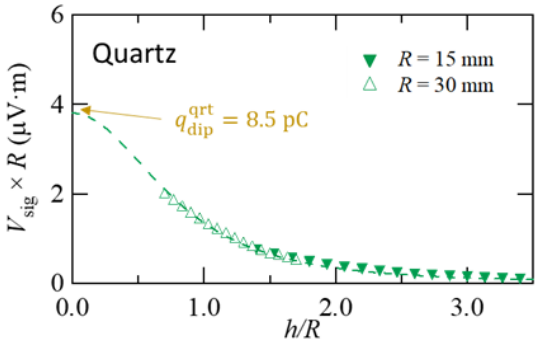

Fig. 5. Signal amplitude multiplied by R as a function of h/R for the quartz sample.

$$+\frac{-\overline{p}(x_1+h)}{\{(x_1+h)^2+x_2^2+x_3^2\}^{3/2}}\Bigg], \tag{4}$$

where h is the distance between the dipole and the metal plate ($h \gg l$). Thus, the ASEM field (electric field) generated at point A on the metal surface [Fig. 4(b)] is expressed by

$$E_1(0, x_2, x_3) = -\left.\frac{\partial V}{\partial x_1}\right|_{x_1=0} = -\frac{\overline{p}}{2\pi\epsilon_0}\frac{a^2-2h^2}{r_A^5}, \tag{5}$$

where $r_{\mathrm{A}} = \sqrt{a^2+h^2}$ is the distance between the charge and point A, and a is the radial coordinate $\sqrt{x_2^2+x_3^2}$ on the metal disk. Accordingly, a surface charge density $\sigma = \epsilon_0 E_1$ is induced on the metal plate, and the total charge Q_0 induced on the metal plate of radius R is

written as

$$\begin{aligned} Q_0 &= \int_0^R \sigma \cdot 2\pi a \cdot da \\ &= \frac{\overline{p}}{R}\left[1 + (h/R)^2\right]^{-3/2}. \end{aligned} \tag{6}$$

The total charge Q_0 multiplied by R is expressed as a function of a single variable h/R by

$$Q_0 \times R = q_{\mathrm{dip}} l \left[1 + (h/R)^2\right]^{-3/2}. \tag{7}$$

The derivative dQ/dt of the surface charge flows as an alternating electric current $i(t)$ in the LCR resonator tuned to ω_0. This electric current is converted to the amplitude V_{sig} of the signal voltage through the input impedance $Z_{\mathrm{in}} = 50\ \Omega$ of the preamplifier. Using $V_{\mathrm{sig}} = Z_{\mathrm{in}}\omega_0 Q_0/2$, the voltage amplitude V_{sig} of the ASEM signal is also expressed as a function of the single variable h/R by

$$\begin{aligned} V_{\mathrm{sig}} \times R &= \frac{q_{\mathrm{dip}} l Z_{\mathrm{in}} \omega_0}{2}\left[1 + (h/R)^2\right]^{-3/2} \\ &= V_0 R \left[1 + (h/R)^2\right]^{-3/2}, \end{aligned} \tag{8}$$

where V_0 corresponds to the signal amplitude for $h/R \to 0$ and $V_0 R$ is independent of the antenna radius R. The scaling behavior of $V_{\mathrm{sig}} \times R$ versus h/R for different R strongly supports the dipole detection model [Fig. 5] and provides convincing evidence for the presence of stress-induced polarization.

The polarization charge q_{dip} is obtained by

$$q_{\mathrm{dip}} = \frac{2V_0 R}{Z_{\mathrm{in}}\omega_0 l} \simeq \frac{2V_0 R}{\pi v_{\mathrm{ac}} Z_{\mathrm{in}}}, \tag{9}$$

where v_{ac} is the acoustic velocity of longitudinal waves (6000 m/s in quartz). From the value of $V_0 R$ for $h/R \to 0$, the induced polarization charge in quartz is estimated to be $q_{\mathrm{dip}}^{\mathrm{qrt}} = 8.5$ pC.

We also attempted to evaluate the piezoelectric coefficient from the induced polarization charge. The piezoelectric response in the acoustically excited area S_{ex} is generally written as a function of frequency, that is, $P_{\mathrm{loc}}(\omega_0) = d_{\mathrm{loc}}(\omega_0) T_{\mathrm{ac}}(\omega_0)$. Using the acoustic force $F_{\mathrm{ac}} = T_{\mathrm{ac}} S_{\mathrm{ex}}$, the piezoelectric response can be rewritten as $q_{\mathrm{dip}}(\omega_0) = d_{\mathrm{loc}}(\omega_0) F_{\mathrm{ac}}(\omega_0)$. The estimated piezoelectric coefficient $d_{\mathrm{loc}}^{\mathrm{qrt}}$ of quartz is 22 pC/N, which is an order of magnitude larger than the reported value of ca. 2 pC/N.[15] One possibility for this difference is that the ASEM signal is enhanced by the mechanical resonance of high-Q materials: at resonance, the applied broad-band ultrasound energy is concentrated into mechanical oscillation at the resonance frequency through mode conversions, and the energy accumulates in the crystal

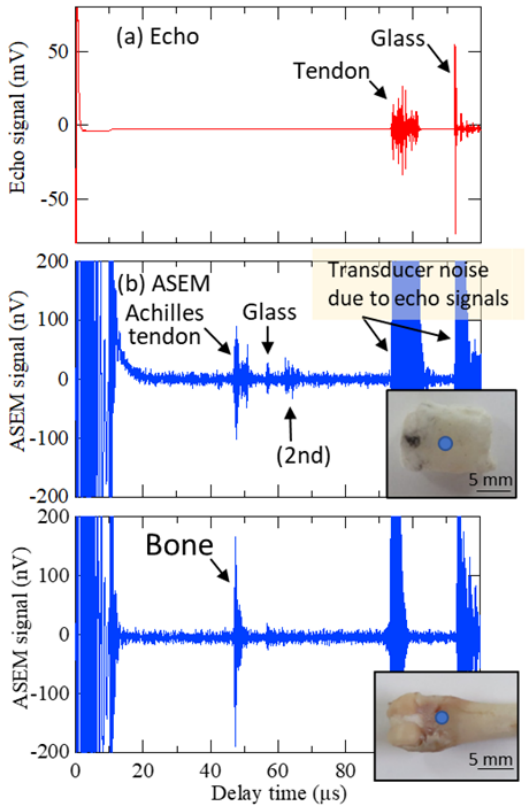

Fig. 6. (a) Time trace of echo signals in Achilles tendon, and time traces of ASEM signals in (b) Achilles tendon and (c) bone (rat femur).[3] The insets show photographs of the samples, where the circles indicate the positions of the measurements. The secondary signal around 65 μs in (b) is attributed to the ASEM response from the tissue induced by ultrasound waves reflected from the glass of the water tank.

over several periods; signal enhancement due to mechanical resonance has also been reported in GaAs (110).[2] The deviation from the reported value may also be attributed in part to the simplification of the model whereby macroscopic polarization is approximated as opposite point charges $\pm q_{\mathrm{dip}}$.

3.2 Acoustically induced electric polarization in biological tissues

Piezoelectricity in biological tissues was first discovered in dehydrated femoral cortex.[9] The microscopic unit of the crystalline structure of bone consists of inorganic hydroxyapatite (HAp) and collagen molecules. Because the unit cell of HAp belongs to a centrosymmetric space group ($P6_3/m$), this inorganic component cannot exhibit piezoelectricity. However, the polypeptide chains in collagen form long rod-like molecules with short-range crystallinity,[16] and this oriented structure makes collagen responsible for the piezoelectricity in bone. This conclusion is supported by the experimental evidence that decollagenized bone (HAp) shows no significant piezoelectric activity.[17,18]

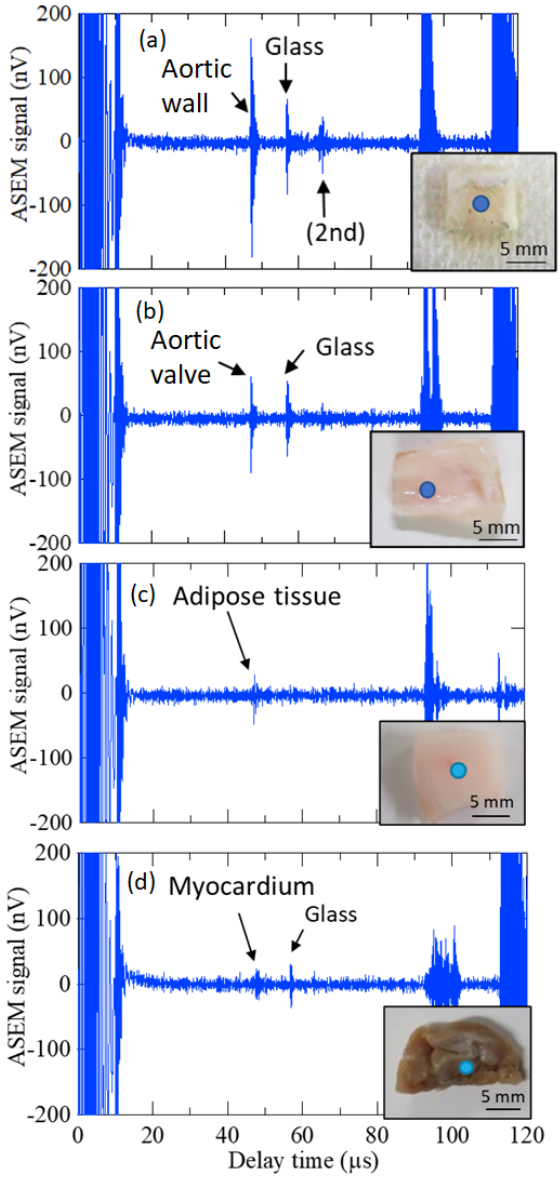

Fig. 7. Time traces of ASEM signals in (a) the aortic wall, (b) the aortic valve, (c) adipose tissue, and (d) the myocardium.[3)]

The presence of piezoelectricity in soft biological tissues was more controversial. The piezoelectric properties of various types of dehydrated biological tissues have been reported, including the Achilles tendon, aortic wall, trachea, and intestines,[10–13)] and the magnitude of their piezoelectric coefficients was estimated to be on the order of 10^{-12} to 10^{-15} C/N. In Ref. 11, a sample of aortic wall was dehydrated under tension for several weeks and a piezoelectric response was observed. In addition to macroscopic piezoelectric properties measured by tensile testing, piezoelectric properties at the nanometer scale have been studied using piezoresponse force microscopy.[19–24)] Surprisingly, aortic walls and their main component

elastin may also be ferroelectric.[23,24] However, Lenz *et al.* found neither piezoelectricity nor ferroelectricity in aortic walls and observed no stress-induced charge.[25] Because the techniques for measuring piezoelectricity in soft biological tissues are limited to tensile testing or nanometer probe microscopy, an alternative method was required to verify the electromechanical properties.

In addition, although electromechanical coupling in wet tissues is more important biologically and medically,[26] it is usually difficult to evaluate the stress-induced charge on wet tissues because of the formation of electric double layers, with high-frequency measurements required to avoid their effect and that of electrochemical transport.[27] Although piezoelectricity in wet bone has been investigated by applying megahertz ultrasound modulation,[2,14,28–30] the piezoelectric properties of wet soft tissues are yet to be addressed.

In previous work, we provided experimental evidence that fibrous biological tissues exhibit stress-induced polarization even when wet.[3] Figures 6(a) and 6(b) show time traces of the echo and ASEM signals for a sample of bovine Achilles tendon; in Fig. 6(b), the signal from the glass of the water tank is also observed around 57 μs because the sample is sufficiently transparent to ultrasound. Similar ASEM signals are observed for samples of bone [Fig. 6(c)], aortic wall [Fig. 7(a)] and aortic valve [Fig. 7(b)], whereas the ASEM signal is small in samples of adipose tissue [Fig. 7(c)] and myocardium [Fig. 7(d)]. These results indicate that fibrous tissues exhibit relatively large piezoelectricity.

The h/R dependences of $V_{\mathrm{sig}} \times R$ for the Achilles tendon and aortic wall are shown in Fig. 8(a), where the signals were measured using two antennas, one with $R = 15$ mm and the other with 30 mm. The signal voltage V_{sig} is scaled well by multiplying it by the antenna radius R, which strongly supports the model of acoustically induced electric polarization. The experimental data are fitted with Eq. (8), and from the values of $V_0 R$, the induced polarization charges for the Achilles tendon and aortic wall are estimated to be $q_{\mathrm{dip}}^{\mathrm{tnd}} = 57$ fC and $q_{\mathrm{dip}}^{\mathrm{artw}} = 90$ fC, respectively. We also investigated the stress dependence of the polarization charge. As shown in Fig. 8(b), the polarization charge q_{dip} exhibits linear behavior in the measurement stress range, thus, d_{loc} is estimated to be roughly 1 pC/N for the Achilles tendon and 2 pC/N for the aortic wall; these values are comparable to the static piezoelectric coefficient (ca. 1 pC/N) reported for a dehydrated tendon or aortic wall.[10,11,23] The basic question about ferroelectricity in aortic walls remains, but our study demonstrates the presence of piezoelectricity in aortic walls and other biological tissues.

In general, the piezoelectric coefficient of a single crystal can be regarded as a specific material parameter that indicates how well it polarizes in response to stress [Fig. 9(a)].

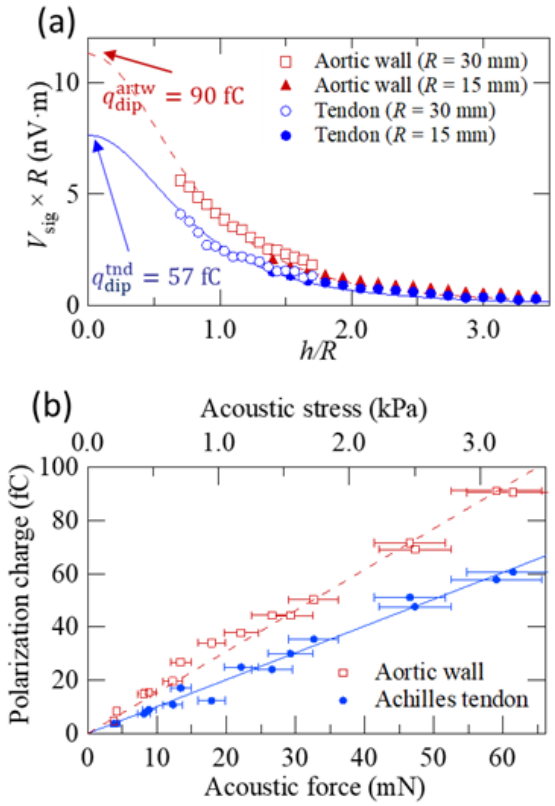

Fig. 8. Quantitative analysis of piezoelectric polarization in biological tissues.[3)] (a) Signal amplitude multiplied by R as a function of h/R for samples of the Achilles tendon and aortic wall. (b) Induced polarization charge q_{dip} as a function of acoustic force F_{ac} for samples of Achilles tendon and aortic wall.

However, in a piezoelectric polycrystal, the stress-induced polarization is attributed to the sum $\overline{p}(t) = \sum_n p_n$ of the electric dipole moments p_n occurring in individual crystal grains [Fig. 9(b)]; therefore, the piezoelectric polarization (or the piezoelectric coefficient) depends largely on the alignment of crystal grains even in the same material. Simply considered, one would therefore expect the acoustically induced polarization in biological tissues to be highly dependent on the alignment of fibrous proteins such as collagen or elastin [Figs. 9(c) and 9(d)]. Figure 10 shows time traces of the ASEM signal in artificial collagen sheets (ca. 300 μm thick).[14)] The ASEM signal of the well-oriented collagen is larger than that of the randomly oriented collagen, suggesting that the signal amplitude is an indicator for assessing the orientation of fibrous tissues.

3.3 Toward medical applications

The ASEM method is characterized by its ability to (i) obtain the spatial distribution of biopiezoelectricity by ultrasound scanning and (ii) evaluate biopiezoelectricity even in living tissues. Therefore, it has potential applications in medical diagnosis of fibrous tissues such as

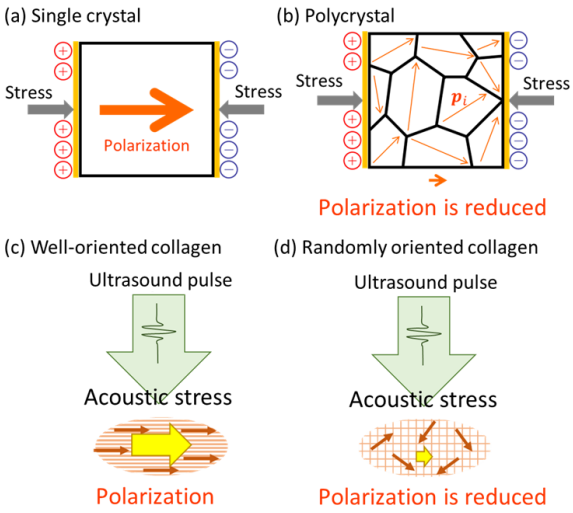

Fig. 9. Schematics of piezoelectric polarization of (a) single crystal and (b) polycrystal of inorganic piezoelectric material, and schematics of acoustically induced polarization of (c) well-oriented collagen and (d) randomly oriented collagen in fibrous tissues.

bones, tendons, and the aortic wall.

One interesting application is the evaluation of bone quality in osteoporosis. Bone strength depends on both quantity and quality: the former is estimated routinely in clinical settings via bone mineral density measurements, but the latter is yet to be evaluated. It is known that collagen fibrous tissues are remodeled to be optimally oriented for mechanical loading (Wolff's law),[31,32] and this idea suggests that collagen orientation could be a new indicator for assessing bone quality. Therefore, we investigated the piezoelectricity of femoral bones in an osteoporosis model (an immobilized rat knee). The right knee of an 8-week-old rat was immobilized with a cast in 150° of flexion for 12 weeks, with the non-immobilized left limb as a control. Echo and ASEM images of bones from the control left limb and the immobilized right limb are shown in Fig. 11. Spatial images were obtained by moving the sample using an XY stage; here, the echo images measured simultaneously with the ASEM images were acquired for sample positioning. In the immobilized limb, a tendency for the ASEM signal of the bone to decrease has been found, especially in the metaphysis. Although as yet unpublished, further recent studies have demonstrated the significance of the reduction in the ASEM signal for 11 rats using a t-test ($p < 0.01$). Thus, the correlation between the induced polarization and collagen orientation in osteoporosis is worth investigating in more detail.

Development for human measurements is also being pursued vigorously [Fig. 12].[33]

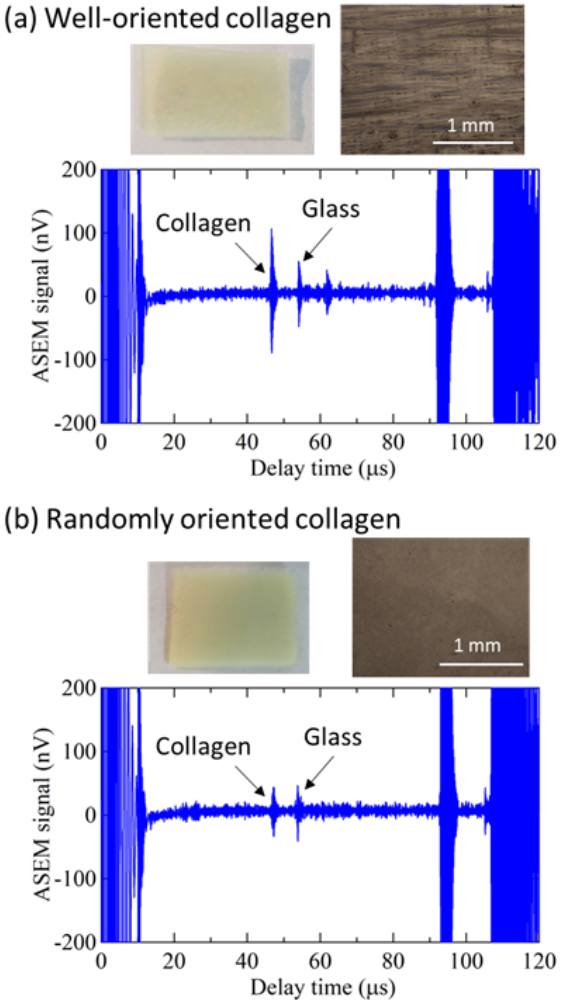

Fig. 10. Time traces of ASEM signal in (a) well-oriented and (b) randomly oriented collagen sheets.[14)]

Because the human body acts as an antenna to receive ambient external radio waves, it is necessary to devise an ASEM detection scheme that avoids the noise from the human body. One important point is to ground the human body in the vicinity of the measurement position [Fig. 12(a)]. Another is to use a differential antenna that detects the difference between the charges induced on the two metal plates [Fig. 12(b)]; a differential antenna is powerful for human measurements because it successfully subtracts common noise caused by external radio waves. Typical time traces of the ASEM signal for a finger and upper arm (53-year-old male) are shown in Fig. 12(a) and 12(b), respectively. From half the echo delay time ($\tau_{\mathrm{echo}}/2$), the signals at 21 μs for the finger (Fig. 12(c)) and at 22 μs for the upper arm [Fig. 12(d)] are identified as the ASEM signal on the bone surface (cortical bone).

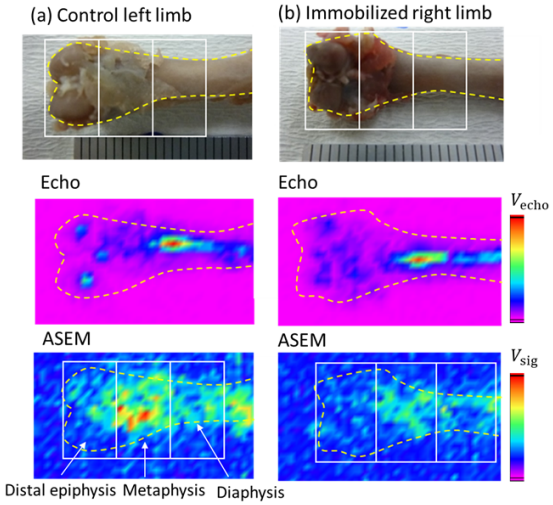

Fig. 11. Photographic (upper), echo (middle) and ASEM (bottom) images of bones from (a) control left limb and (b) immobilized right limb.

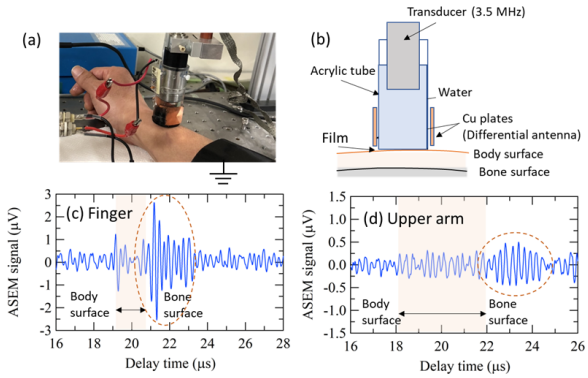

Fig. 12. Human measurements. (a) Photograph of the measurement setup. (b) Schematic of an ASEM probe integrated with an ultrasound transducer (3.5 MHz) and a differential Cu-plate antenna. Time traces of ASEM signal for (c) finger and (d) upper arm.

4. Acoustically induced magnetic polarization

4.1 Magnetic imaging via ultrasound

To detect rf magnetic fields generated by acoustically induced magnetic polarization, the inductance L —which constitutes a resonant circuit tuned to the ultrasound frequency —is used as a loop antenna (pickup coil). Magnetic imaging via ultrasound has been performed by using the ASEM response [Fig. 13)].[4)] The samples were positioned on the bottom of a glass beaker, and well-defined signal was observed from ferrite but no signal was detected from nonmagnetic material (Cu). Interestingly, a weak signal along the sample edges of pure iron

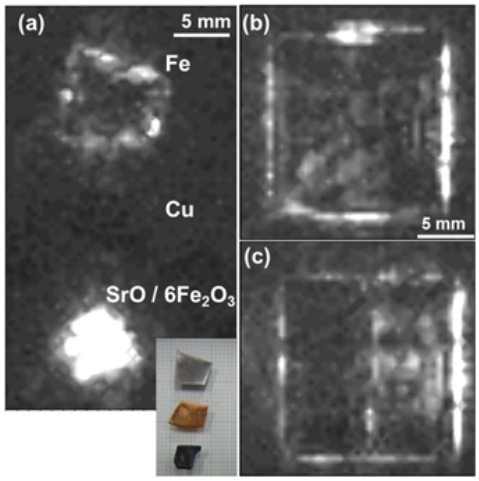

Fig. 13. Magnetic images obtained by ultrasound scanning.[4] (a) ASEM images of different magnetic materials. The inset is a photograph of the samples (pure iron and copper foils, and a flake of $SrO/6Fe_2O_3$). ASEM images of the iron foil (b) before and (c) after folding.

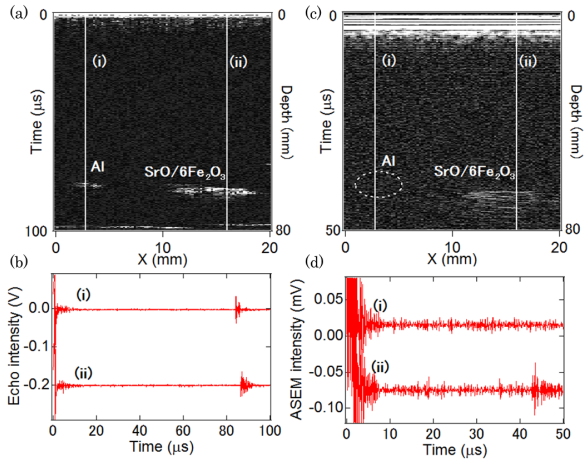

Fig. 14. Tomographic images of a gel phantom embedded with aluminum and ferrite flakes.[4] (a) Echo tomographic image (B-mode). (b) Time traces of echo signal at two positions, indicated by the white lines (i) and (ii) in (a). (c) ASEM tomographic image, measured simultaneously with the echo measurements. (d) Time traces of ASEM signal.

foil is observed. Figure 13(b) shows the detailed profiles of ASEM imaging for pure iron foil, suggesting the presence of magnetization along the sample edges. Because net magnetization is not expected in soft magnetic iron, we assume that the signal arises from the aligned domains induced by external stress or distortion when the iron foil is cut. When an external distortion is applied by folding the foil in the middle, the signal is observed along the folded line [Fig. 13(c)]. This finding provides valuable hints for nondestructive evaluation (NDE) of residual

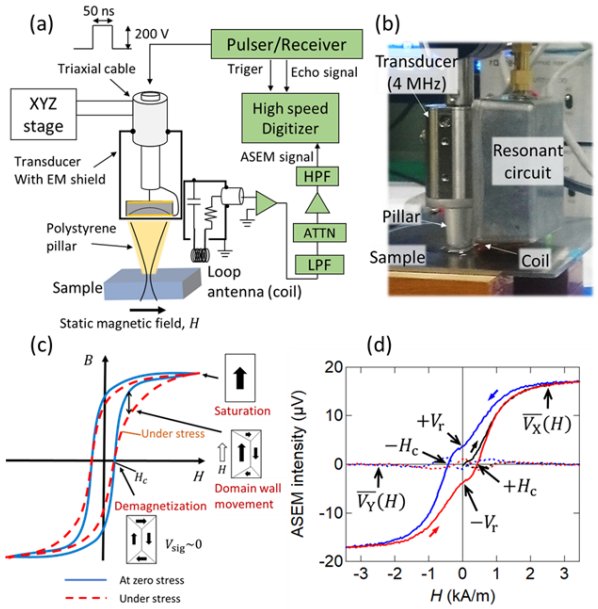

Fig. 15. (a) Block diagram and (b) photograph of the measurement setup for nondestructive evaluation of steel. (c) Standard magnetic hysteresis curve (B - H curve). (d) Typical ASEM hysteresis curve in steel.[36,37] Here,the in-phase component $\overline{V}_X$ (solid line) and the quadrature component $\overline{V}_Y$ (dotted line) were obtained by phase-sensitive detection.[35,36] The black, blue, and red lines represent the initial magnetization curve, the downward-field curve, and the upward-field curve, respectively.

stress in steel, which we discuss in Sec. 4.3.

Tomographic images are shown in Fig. 14 from several flakes of nonmagnetic aluminum and magnetic ferrite implanted into a gel phantom. The magnetic flakes (ferrites) are easily distinguished in ASEM tomography [Fig. 14(c)], whereas all flakes appear similar in echo tomography (corresponding to B-mode) [Fig. 14(a)]. Therefore, the ASEM method may be used for magnetically selective noninvasive sensing.

4.2 Magnetic hysteresis measurements via ultrasound

All ferromagnetic materials exhibit hysteresis in their variation of flux density $\boldsymbol{B}$ with magnetic field $\boldsymbol{H}$. Hysteresis properties such as permeability, coercivity, remanence, and hysteresis loss are known to be sensitive to factors such as stress, strain, grain size, and heat treatment. Because hysteresis measurements yield a number of independent material parameters, they have been used to determine material properties in the NDE of steel and various types of infrastructure. Therefore, it is important to clarify the hysteresis properties of the ASEM response.

Figure 15 shows the measurement setup and a typical hysteresis curve of the ASEM signal in steel.[36,37] ASEM measurements were performed using a 4-MHz focusing transducer with

a delay medium (a 27-mm-long polystyrene pillar) to separate the transducer excitation pulse from the ASEM signal. The signal was detected by a resonant loop antenna tuned at 4.1 MHz. The sample (a 25-mm-thick plate of S25C carbon steel) was subjected to an external magnetic field by using a commercial electromagnet.

To complete the description of magnetic hysteresis under acoustic stress, there must be a constitutive relationship among the magnetic field $\boldsymbol{H}$, the magnetic flux density $\boldsymbol{B}$, and the stress $\boldsymbol{T}$. The magnetic flux is expressed by a nonlinear function, that is, $\boldsymbol{B} = \boldsymbol{F}(\boldsymbol{H}, \boldsymbol{T}) = \mu_0 \boldsymbol{H} + \boldsymbol{M}(\boldsymbol{H}, \boldsymbol{T})$, and the phenomenon of hysteresis implies that the magnetization $\boldsymbol{M}(\boldsymbol{H}, \boldsymbol{T})$ is not a single-valued function of $\boldsymbol{H}$ and $\boldsymbol{T}$ [Fig. 15(c)]. For small reversible changes in the linear response regime, magnetostriction is phenomenologically equivalent to piezomagnetism,[6] and the piezomagnetic coefficient d_{mi} can be defined by

$$d_{mi} = (\partial B_m / \partial T_i)_H = \mu_0 (\partial M_m / \partial T_i)_H. \tag{10}$$

When acoustic stress $T_i(t)$ is applied through ultrasonic irradiation, the magnetic flux density B_m in the material is modulated temporally as follows:[34]

$$\frac{dB_m}{dt} = \mu_0 \left(\frac{\partial M_m(H_m, T_i)}{\partial T_i} \right)_H \frac{dT_i}{dt} = d_{mi}(H) \frac{dT_i}{dt}. \tag{11}$$

Note that the ASEM response arises from the intrinsic magnetic flux (magnetization) confined in a ferromagnetic material and not from leakage flux from the surface of the material into the air; this latter type is detected by the standard flux leakage technique for NDE.

If $\boldsymbol{H}$, $\boldsymbol{B}$, and $\boldsymbol{M}$ are axial vectors parallel to the 3-axis in a ferromagnetic material, then the nonzero piezomagnetic coefficients are limited to $d_{31} = d_{32}$ and d_{33} in the uniaxial symmetry of a polycrystalline medium. When the wave vector $\boldsymbol{k}$ of longitudinal ultrasound waves is parallel to the 1-axis, the signal voltage $V_{\mathrm{sig}}(H, t)$, detected by a loop antenna, can be expressed as

$$V_{\mathrm{sig}}(t, H) = \eta (dB_3/dt) = \eta d_{31}(H)(dT_1/dt), \tag{12}$$

where η is the detection efficiency in the measurements. Consequently, the magnetic-field dependence of the signal intensity can be identified with that of the piezomagnetic coefficient $d_{31}(H) = (\partial B_3 / \partial T_1)_H$.

In general, the piezomagnetic coefficient can be extended to a complex number.[35] When the acoustic stress, $T_{\mathrm{ac}}(\omega_0) = T_0 e^{-i\omega_0 t}$, is applied to a local area in a material, the induced flux density is written as $B(\omega_0, H) = B_0(H) e^{-i(\omega_0 t - \delta(H))}$, where $\delta(H)$ is the phase delay of B with respect to T_{ac}. From the ratio of $B(\omega_0, H)$ and $T_{\mathrm{ac}}(\omega_0)$, the local piezomagnetic coefficient

$d_{\rm loc}(H)$ at ω_0 is expressed as

$$\begin{aligned} d_{\rm loc}(H) &= \frac{B_0(H)}{T_0}[\cos\delta(H) + i\sin\delta(H)] \\ &= d'(H) + d''(H). \end{aligned} \tag{13}$$

The phase delay δ gives rise to the imaginary part d'' characterizing the energy loss at ω_0.

Next, we describe the relationship between the ASEM signal and the complex piezomagnetic coefficient. The Fourier component $V_{\rm sig}$ is written as

$$\begin{aligned} V_{\rm sig}(\omega, H) &= -i\eta\omega B(\omega, H) \\ &= -i\eta\omega d(\omega, H)T_{\rm ac}(\omega) \\ &= \eta\omega[d''(\omega, H) - id'(\omega, H)]T_{\rm ac}(\omega), \end{aligned} \tag{14}$$

where $V_{\rm sig}(\omega, H)$ has a quadrature phase shift with respect to $B(\omega, H)$ induced in a material. Consequently, for a sinusoidal wave, $T_{\rm ac}(\omega_0) = T_0 e^{-i\omega_0 t}$, the first harmonic component of $V_{\rm sig}(\omega_0, H)$ is expressed as

$$V_{\rm sig}(\omega_0, H) = \eta\omega_0 B_0(H) e^{-i(\omega_0 t - \delta(H) - \phi + \pi/2)}, \tag{15}$$

where ϕ is the adjustable phase shift attributed to the measurement system. Using a phase-sensitive detection (PSD) scheme, we separate $V_{\rm sig}(\omega_0, H)$ into the in-phase component V_X (real part) and the quadrature component V_Y (imaginary part). When ϕ is tuned to $\pi/2$, these components are written as $V_X = \eta\omega_0 T_0 d'(\omega_0, H)$ and $V_Y = \eta\omega_0 T_0 d''(\omega_0, H)$. The in-phase component ($V_X \propto d'$) is a quasi-static property with respect to magnetomechanical effects, and the quadrature component ($V_Y \propto d''$) is attributed to energy dissipation processes at ω_0 such as microscopic eddy currents induced by domain wall movement.

In the hysteresis measurements, the signal voltages were plotted as the in-phase component $\overline{V}_X$ and the quadrature component $\overline{V}_Y$ integrated between $\tau_{\rm echo}/2$ and $\tau_{\rm echo}/2+\Delta t$ in the ASEM waveform after PSD [Fig. 15(d)].[35–37] The coercivity H_c and the remanent magnetization signal $V_r \propto d'(H = 0)$ are determined from the intercepts of the transverse and longitudinal axes in the $\overline{V}_X(H)$ hysteresis loop, respectively. The signal voltage V_r is the ASEM intensity arising from the remanent magnetization. We also introduce two parameters: the area W of the hysteresis loop and the initial slope m_0 of the initial magnetization curve. The area is written as $W = \oint \overline{V}_X(H)dH \propto \oint d'(H)dH = \oint \frac{dB}{dT}dH \approx \frac{d}{dT}\oint BdH = \frac{d}{dT}W_{B-H}$, where W_{B-H} corresponds to the hysteresis loss in the standard B - H curve. Similarly, the initial slope is written as $m_0 = \frac{d}{dH}\overline{V}_X \propto \frac{d}{dH}d' = \frac{d^2}{dHdT}B \approx \frac{d}{dT}\mu'$, where μ' is the real part of the complex permeability. These four hysteresis parameters are fingerprint information that characterizes

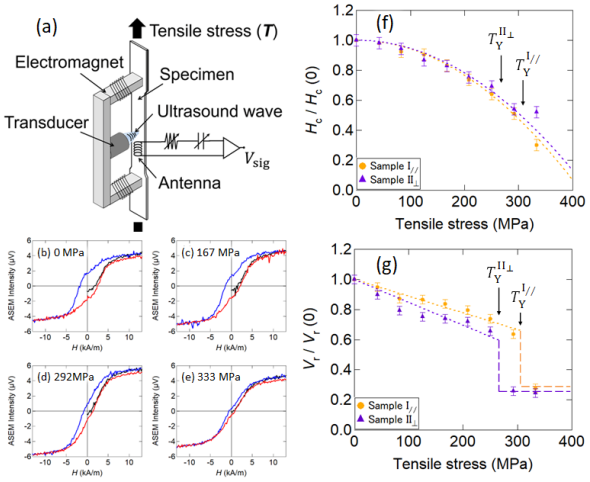

Fig. 16. (a) Schematic of the *in situ* measurement setup for tensile testing.[36] Hysteresis curves at (a) 0 MPa, (b) 167 MPa, (c) 292 MPa, and (e) 333 MPa. The data in (e) show the hysteresis curve in the plastic region beyond the yield stress point, T_Y. Stress dependence of (f) normalized coercivity, $H_c/H_c(T=0)$ and (g) normalized remanent signal, $V_r/V_r(T=0)$. The dotted lines show the best-fit curve below the yield stress points. Recrystallization and grain deformation occur during the rolling process of steel making, and the alignment of grains may cause mechanical and magnetic anisotropies. Therefore, we prepared two samples ($I_{//}$ and $II_\perp$) whose rolling directions were parallel and perpendicular to the direction of tensile stress, respectively.

ferromagnetic materials.

In standard carbon steel, the quadrature component $\overline{V}_Y \propto d''$ is almost negligible at the ultrasound frequency ω_0 in the rf range. However, in impurity-rich iron oxides [e.g., an iron oxide layer (mill scale) formed in the manufacturing of hot-rolled steels, consisting mainly of magnetite (Fe_3O_4)], an anomalous sharp peak is observed in the hysteresis curve of $\overline{V}_Y$.[35] Interpreted from the Debye model with a single relaxation time, the maximum of $\overline{V}_Y$ implies that the relaxation time τ of the spin system becomes closer to the ultrasound timescale, that is, $\omega_0\tau \simeq 1$, probably because of domain wall movement with pinning on defects.

4.3 Toward industrial applications

The fact that local magnetic hysteresis curves can be obtained by ultrasound focusing indicates that the spatial distribution of magnetic flux density and various hysteresis parameters can be mapped nondestructively. Therefore, magnetic sensing by the ASEM method is expected to be applied to a wide range of industrial fields, particularly in the NDE of steel. Using the ASEM method, we have demonstrated the evaluation of embrittlement in austenitic stainless steel,[4] flaw detection in steel,[5,38] and the evaluation of rebar corrosion in reinforced concrete.[39]

Here, we present an interesting application: quantitative evaluation and imaging of residual stress in steel. Undesirable residual stress is usually introduced during steel manufacturing,

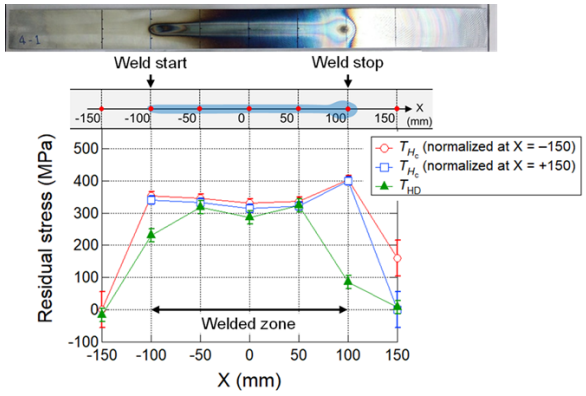

Fig. 17. Profiles of residual stress converted from coercivity (T_{H_c}) and stress values estimated from strain relaxation in the hole-drilling (HD) method (T_{HD}).[37] Two profiles obtained by choosing the coercivity at $X = -150$ mm and 150 mm as the normalization factor $H_c(0)$ are plotted. The weld start and stop locations correspond to $X = -100$ mm and 100 mm, respectively. The upper panel shows a photograph of the side opposite to the welded face of the steel specimen.

product fabrication, and welding. When service stress is combined with initial residual stress, the concentration of tensile stress may damage engineering components, and to avoid that risk, it is important to understand the stress distribution in actual objects. The residual stress is usually obtained by measuring strain relaxation with the destructive sectioning method[40] or semidestructive hole-drilling (HD) method.[41] Although X-ray diffraction allows the NDE of residual stress, that method is limited to steels with small crystal grains.[42] There have been extensive studies on the effects of residual stress involving ultrasound,[43] magnetic hysteresis loop,[44–47] and Barkhausen noise (BN) measurements[44,48–50] for the NDE of residual stress. However, the quantitative evaluation and spatial imaging of residual stress are still under development.

Magnetic hysteresis parameters such as coercivity and remanent magnetization are sensitive to stress in ferromagnetic materials. This suggests that hysteresis parameters can be used as indicators for evaluating residual stress in steel. We investigated the stress dependence of local hysteresis loops via the ASEM response using a tensile testing machine [Fig. 16].[36] The hysteresis curves clearly depended on the applied tensile stress [Fig. 16(b) - 16(e)], and the stress dependences of normalized coercivity $H_c/H_c(T = 0)$ and normalized remanent signal $V_r/V_r(T = 0)$ are shown in Fig. 16(f) and 16(g), respectively. We fitted the characteristic stress curves of the normalized hysteresis parameters with a polynomial function of the stress T, that is, $1 + C_1T + C_2T^2$ with a single fitting parameter for H_c ($C_1 = 0$) and for V_r ($C_2 = 0$), and the best-fit parameters in the elastic region were $C_2 = -5.83 \times 10^{-18}$ Pa^{-2} for H_c and

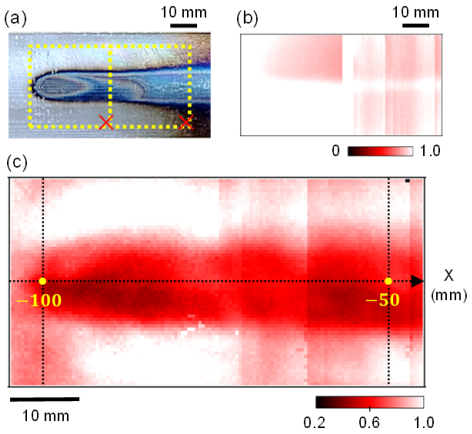

Fig. 18. Imaging of residual stress through the ASEM response in steel.[37](a) Photograph of the side opposite to the welded face near the weld start location. A yellow dotted square indicates the scanning area for a single measurement performed in the same setting (one area: 30 mm × 30 mm). The signal intensity is normalized by that at the position marked by the red cross in each scanning area. (b) Image of normalized echo intensity. (c) Image of normalized V_r.

$C_1 = -1.11 \times 10^{-9}$ Pa^{-1} for V_r in the sample I$_{//}$.[36]

We demonstrated the evaluation and spatial imaging of tensile residual stress through local hysteresis parameters using a welded steel specimen [Fig. 17 and Fig. 18].[37] The specimen was partially welded along the center line on one side of the steel plate. Because the welded face contracts after heating, tensile residual stress is expected to be generated on the opposite face (the upper panel in Fig.17). First, local hysteresis curves of the ASEM signal were measured at seven positions on the side opposite to the welded face (red solid circles in the schematic of the specimen in Fig. 17). From the hysteresis loop of the in-phase component $\overline{V}_X$, coercivity is obtained at individual positions. A one-dimensional profile of residual stress T_{H_c} along the welded zone is obtained using the stress-coercivity conversion function, $H_c/H_c(0) = 1 + C_2T^2 = 1 - 5.83 \times 10^{-18}T^2$ [Fig. 17], where $H_c(0)$ is the coercivity measured outside the welded zone ($X = -150$ mm or 150 mm). In the center part of the welded zone (-50 mm $\leq X \leq$ 50 mm), the residual stress T_{H_c} converted from coercivity is sufficiently consistent with the stress T_{HD} estimated by the HD method. However, a large discrepancy between T_{H_c} and T_{HD} is observed especially at the weld stop location ($X = 100$ mm). The discrepancy can be explained as being due to plastic deformation, which is supported by the electron backscatter diffraction method.[37] In plastic deformation, the internal stress is released by the rearrangement of crystal grains. Although the plastically deformed region is usually undetected in the HD method, the history of excessive stress applied beyond T_Y is

firmly recorded by the magnetic parameters even after the internal stress is released.

Figure 18 shows the imaging results of residual stress through ASEM response. High-contrast images of the welded zone were obtained using V_r [Fig. 18(c)], while uniform images were observed by standard echo signals [Fig. 18(b))]. The red area in Fig. 18(c) indicates the region of high residual stress. Estimating stress values from the conversion function $V_r/V_r(0) = 1 + C_1T = 1 - 1.11 \times 10^{-9}T$, the dark red area suggests a plastically deformed region where excessive local stress was previously applied beyond T_Y.[37)]

We propose a guideline for NDE of tensile residual stress using the ASEM method. First, a magnetic field is applied until the magnetization saturates in the area of steel to be measured. The field is then decreased gradually to zero. Next, V_r images are scanned within the area under fixed measurement conditions. This process screens for plastically deformed or at-risk areas with high residual stress. For at-risk areas, the coercivity is measured from the ASEM hysteresis loop to confirm the stress value quantitatively. Note that the hysteresis parameters H_c and V_r must be normalized with respect to the values at which zero stress is expected.

5. Summary

The main origins of ASEM response are classified into stress-induced electrical polarization due to piezoelectricity (and also due to ferroelectricity) and stress-induced magnetic polarization due to ferromagnetism.

For the stress-induced electric polarization, we have succeeded in imaging and quantitatively evaluating piezoelectricity in biological tissues, opening a new way to explore biopiezoelectricity. More recently, we have been investigating the relationship between biopiezoelectricity and disease, such as the reduction of piezoelectric polarization due to osteoporosis in a rat model. Although this research has just begun, it is not limited to basic research on biopiezoelectricity. We plan to develop a human measurement system and apply it to medical applications.

We have also been working on stress-induced magnetic polarization from early on because it is relatively easy to formulate the ASEM phenomena and there is a clear need for it from industry. We have demonstrated magnetic imaging, magnetic hysteresis measurement and evaluation of magnetic relaxation time, providing three important elements of measurement technology: imaging, quantification, and dynamics evaluation. The technology is now being transferred to related companies for use in the NDE inspection of infrastructure and steel.

Acknowledgment

This work was supported by JSPS grants-in-aid (nos. 20H04500 and 22K19912).

We are grateful to H. Yamada, N. Ohno, S. Naito, K. Watanabe, T. Kumamoto, and Y. Anzai from Tokyo University of Agriculture and Technology (TUAT) for assistance in the early stages of this work. We are also grateful to Y. Yabe and Y. Hagiwara from the Department of Orthopaedic Surgery, Tohoku University, and N. Niimi, Y. Kojima, and M. Mori from Nippon Sigmax Co., Ltd. for collaboration on experiments of osteoporosis rat models. We would like to thank J. Yotsuji from JFE Steel Corporation and Y. Suzuki from IHI inspection & Instrumentation Co., Ltd. for collaboration on experiments of steel and useful information on the needs of industrial fields. We would also like to thank N. Kaitoh, Y. Enomoto, J. Kikuchi, Y. Sakakura and K. Ito from TUAT, K. Tamura from Hamamatsu University School of Medicine, and M. Matsukawa from Doshisha University for collaboration on human measurements and for simulating discussion on biological tissues.

References

1) For instance, *Physical Acoustics* (Academic Press, New York, 1964) Vol. 1-4.
2) K. Ikushima,S. Watanuki, and S. Komiyama, Appl. Phys. Lett. **89**, 194103 (2006).
3) K. Ikushima, T. Kumamoto, K. Ito, and Y. Anzai, Phys. Rev. Lett. **123**, 238101 (2019).
4) H. Yamada, K. Takashima, K. Ikushima, H. Toida, M. Sato, and Y. Ishizawa, Rev. Sci. Instrum. **84**, 044903 (2013).
5) H. Yamada, K. Watanabe, and K. Ikushima, Jpn. J. Appl. Phys. **54**, 086601 (2015).
6) D. A. Berlincourt, D. R. Curran, and H. Jaffe, *Physical Acoustics* (Academic press, New York and London, 1964), vol.1 part A, pp. 169-270.
7) W. G. Cady, *Piezoelectricity* (Mc Graw-Hill Co., New York, 1946), p. 806.
8) J. Duchesne, J. Depireus, A. Bertinchamps, N. Comet, and J. M. Van der Kaa, Nature (London) **188**, 405 (1960).
9) E. Fukada and I. Yasuda, J. Phys. Soc. Jpn. **12**, 1158 (1957).
10) E. Fukada and I. Yasuda, Jpn. J. Appl. Phys. **3**, 117 (1964).
11) E. Fukada and K. Hara, J. Phys. Soc. Jpn. **26**, 777 (1969).
12) E. Fukada, Biorheology **32**, 593 (1995).
13) E. Fukada, Adv. Biophys. **6**, 121 (1974).
14) K. Ikushima, H. Yamada, N. Niimi, Y. Kojima, Y. Yabe, and Y. Hagiwara, Proc. IEEE Int. Ultrasonics Symp., 2018 (10.1109/ULTSYM.2018.8579666).
15) E. Fukada, IEEE Trans. Ultrason. Ferroelectr. Freq. Control **47**, 1277 (2000).
16) M. D. Shoulders and R. T. Raines, Annu. Rev. Biochem. **78**, 929 (2009).
17) A. A. Marino, S. C. Sodertholm, and R. O. Becker, Calc. Tiss. Res. **8**, 177 (1971).
18) Polar crystalline phases such as $P6_3$ and $P2_1/b$ are also suggested by the X-ray diffraction pattern of decollagenized bone (HAp). Hence, the piezoelectricity of HAp has been studied by piezoresponse force microscopy but the piezoelectric response of HAp was much smaller than that of decalcified bone (collagen): Y. Zhang, A. A. Gandhi, J. Zeglinski, M. Gregor, S. A. M. Tofail, IEEE Trans. Dielectr. Electr. Insul, **19**, 1151 (2012).
19) S. V. Kalinin, A. Rar, and S. Jesse, IEEE Trans. Ultrason. Ferroelectr. Freq. Control **53**, 2226 (2006).
20) A. Gruverman and S. V. Kalinin, J. Mater. Sci. **41**, 107 (2006).
21) S. V. Kalinin *et al.*, Annu. Rev. Mater. Res. **37**, 189 (2007).
22) D. A. Bonnel *et al.*, MRS Bull. **34**, 648 (2011).

23) Y. Liu, Y. Zhang, M-J. Chow, Q. N. Chen, and J. Li, Phys. Rev. Lett. **108**, 078103 (2012).
24) Y, Liu, H.-L. Cai, M. Zelisko, Y. Wang, J. Sun, F. Yan, F. Ma, P. Wang, Q. N. Chen, H. Zheng, X. Meng, P. Sharma, Y. Zhang, and J. Li, Proc. Natl. Acad. Sci. U.S.A. **111** (27), E2780-E2786 (2014).
25) T. Lenz, R. Hummel, llias Kastsouras, W. A. Groen, M. Nijemeisland, R. Ruemmler, M. K. E. Schäfer, and D. M. de Leeuw, Appl. Phys. Lett. **111**, 133701 (1-5) (2017).
26) C. A. L. Bassett, Calc. Tiss. Res. **1**, 252-272 (1968).
27) A. C. Ahn and A. J. Grodzinsky, Med. Eng. Phys. **31**, 733 (2009).
28) M. Okino, S. Coutelou, K. Mizuno, T. Yanagitani, and M. Matsukawa, Appl. Phys. Lett. **103**, 103701 (2013).
29) H. Tuneda, S. Matsukawa, S. Takayanagi, K. Mizuno, T. Yanagitani, and M. Matsukawa, Appl. Phys. Lett. **106**, 073704 (2015).
30) S. Matsukawa, T. Makino, S. Mori, D. Koyama, S. Takayanagi, K. Mizuno, T. Yanagitani, and M. Matsukawa, Appl. Phys. Lett. **110**, 143701 (2017).
31) J. Wolff, Virchovs Archiv, **50**, 389-453 (1870).
32) R. B. Martin, D. B. Burr, N. A. Sharkey, *Skeletal Tissue Mechanics* (Springer, New York, 2015) Ch. 8, pp. 309.
33) Institutional Review Board (IRB)/Ethics Committee approval was obtained from Tokyo University of Agriculture and Technology, Japan. All subjects enrolled in this study signed a written consent form before initiation of the study-specific procedures.
34) O. Hubert and K.-J. Rizzo, J. Magn. Magn. Mater. **320**, e979 (2008).
35) H. Yamada, J. Yotsuji, and K. Ikushima, Jpn. J. Appl. Phys. **57**, 07LB09 (2018).
36) Y. Suzuki, H. Yamada, and K. Ikushima, IEEE Trans. Ultrason. Ferrolectr. Freq. Control **67**, 825 (2020).
37) Y. Suzuki, D. Hosokawa, and K. Ikushima, IEEE Trans. Ultrason. Ferrolectr. Freq. Control **69**, 1478 (2022).
38) J. Yotsuji, K. Ikushima, and H. Yamada, ISIJ international **60**, 948 (2020).
39) M. Uehara, M. Kuroda, H. Yamada, Y. Kawano, and K. Ikushima, Proc. 37th Symp. Ultrasonic Electronics, 2P2-9 (2016).
40) N. Tebedge, G. Alpsten, and L. Tall, Exp. Mech. **13**, 88 (1973).
41) B. Zuccarello, Exp. Mech. **39**, 117 (1999).
42) I. C. Noyan and J. B. Cohen, *Residual Stress: Measurement by Diffraction and Interpretation* (New York, NY, USA: Springer, 1987) pp. 94.
43) T. Leon-Salamanca and D. F. Bray, Res. Nondestruct. Eval. **7** 169 (1996).

44) D. Jiles, *Introduction to Magnetism and Magnetic Materials* (3rd ed. Boca Raton, FL, USA: CRC Press, 2016) p. 421.
45) S. Abuku and B. D. Cullity, Exp. Mech. **11**, 217(1971).
46) S. Abuku, Jpn. J. Appl. Phys. **16**, 1161 (1977).
47) J. M. Makar and B. K. Tanner, J. Magn. Magn. Mater. **222**, 291 (2000).
48) A. Mitra, L. B. Sipahi, M. R. Govindaraju, D. C. Jiles, and V. R. V. Ramanan, J. Magn. Magn. Mater. **153**, 231 (1996).
49) S. Desvaux, M. Duquennoy, J. Gualandri, and M. Ourak, NDT & E Int. **37** 9 (2004).
50) H. I. Yelbay, I. Cam, and C. H. Gür, NDT & E Int. **43**, 29 (2010).